Mono- and multi-diameter approaches to predict stratified flow structure by means of CFD simulations in DAF systems

Dmytro Hlukhov, Gorka S. Larraona [*], Alejandro Rivas, Juan Carlos Ramos

Universidad de Navarra, TECNUN Escuela de Ingeniería, Departamento de Ingeniería Mecánica y Materiales, Manuel de Lardizábal 13, 20018 San Sebastián, Spain

ARTICLE INFO

ABSTRACT

This paper presents a Computational Fluid Dynamics (CFD) model of a pilot scale dissolved air flotation (DAF) tank. A Multiphase Mixture model was used to analyse the influence of bubble sizes on the formation of a stratified flow structure. Critical bubble diameter is defined as the size of the bubble that implies the equality of the bubble rising velocity and flow downward velocity in the separation zone (SZ). The fact as to whether using air bubble sizes which are greater or less than the critical diameter value significantly affects the air content, flow structure and the limit of the whitewater blanket inside the SZ is assessed. The study was carried out using two approaches, namely, mono- and multi-diameter. The results obtained via the mono-diameter approach proved to be closely in line with experimental data when air concentration in the SZ had almost, but not quite, a constant value. However, it failed to predict the case of the progressive decrease in air below half of SZ height. A combined effect of bubbles with different rising speed was required to reproduce a smooth air profile curve, as measured experimentally. In this context, a multi-diameter approach is deemed to be a suitable method for reproducing the stratified structure. In addition, this approach offers the chance to study bubble size distribution inside the SZ domain.

1. Introduction

Dissolved air flotation (DAF) is well known for its ability to eliminate low specific gravity particles such as algae (e.g. Cryptosporidium and Giardia) and to treat low turbidity raw water [1]. The DAF tank comprises two main parts separated by means of a baffle: the contact zone (CZ) and the separation zone (SZ). Part of the clarified water is recycled into the saturation equipment, with the purpose of being saturated with air. Lately, this recycled current has been depressurized in the contact zone by mean of injectors, producing a cloud of microbubbles (MB). Aggregates, which are formed in the CZ from the combination of MB and solid particles, are separated from the main current in the SZ due to their density difference. Further information about DAF functioning can be found in [2–4].

Lundh et al. [5–10] carried out a significant number of experiments using a pilot scale DAF tank, with the authors having collected the most complete, detailed and reliable data about DAF functioning, although MB size was not measured. Lundh [7] observed the existence of stratified flow structure in certain operating conditions, reporting that this phenomenon may have a crucial impact on DAF performance. Therefore,

the role of air bubbles is not only limited to solid particle collection, but also to modifying the flow structure inside the SZ. Amato and Wicks [11] reported successful duplication of the water treatment capacity of the plant studied according to this phenomenon, this last statement reflecting the importance of understanding how and why the stratified structure is formed.

A typical MB diameter that can be found in DAF application ranges between 10 and 150 μm [4], with MB size being one of the key parameters affecting DAF performance [12,13]. Macro bubbles (defined by Rykaart and Haarhoff [14] as greater than 150 μm) should be avoided because their rising velocity is high enough to damage or even destroy bubble-particle aggregates. In addition, residence time of these bubbles is too short to effectively collect solid particles. On the other hand, small bubbles may be dragged into the subnatant collection tube and deposited on the sand filter surface afterwards, which means that the number of filter backwashing cycles will increase [2].

Net hydraulic loading (HL) is defined as total (treated + recycled) flow rate divided by the projected area of the SZ, and formed the basis for conventional analysis of the DAF separation zone [15]. This simplified approach is based on a comparison of the rising velocity of the

bubbles and HL. All of the bubbles whose rising speed is greater than the HL are prone to leaving the SZ domain (and therefore the solid particles) through the free surface.

Despite the fact that experimental studies can provide reliable data for optimization of DAF, they are expensive and complex to conduct [8,10,16]. An additional difficulty with pilot scale plants is the complexity involved in scaling the bubble diameter. Reliable in-situ measurement of the most important parameters such as mixture velocity, air concentration and MB size distribution are difficult to take due to the complexity of the experiment and multiphase system characteristics. In this context, Computational Fluid Dynamics (CFD) emerges as an alternative to the traditional methods, having been used to develop [17] and optimize [18] different equipment in the flotation process and found to be a very useful tool in order to predict hydraulic behaviour in water and wastewater treatment [19].

Dissolved air flotation involves a three-phase multiphase flow. However, Lundh [6] reported that for dilute suspended solid concentration (< 25 mg SS/l in the incoming water) flow structure was not affected by the existence of biological flocs. Therefore, most CFD studies [11,20–24] have not taken the solid particles and aggregates into account.

Amato and Wicks [11] carried out CFD simulations in order to upgrade an existing DAF design, which involved constructing 2D and 3D models consisting of 335,000 hexahedral cells. However, the authors gave preference to the 2D model. For its part, the Euler-Euler approach was used with bubble sizes ranging between 70 and 100 μm, and the impact of length-to-height ratio of the inclined baffle and recirculating flow pattern on the SZ were studied. The limit of the whitewater blanket, below which a major decrease in air concentration can be found, is commonly known as the white water level (WWL), and in their studies, Amato and Wicks [25] defined WWL as being with an air fraction limit of 10^{-4}. Authors pointed out that, if WWL was lower than the position of the collection tubes, the quality of the subnatant water could be put at risk, and so it is therefore important to control this parameter.

Bondelind et al. [20,26] researched one and two-phase flows in Lundh's pilot DAF tank using the Euler-Lagrange approach, reporting good reproduction of the flow field in the SZ. The prediction of the water velocity field in single-phase simulations was in line with experimental results, although a discrepancy between the air volume fraction predicted and experimental data was found in the case of two-phase flow simulations. Authors carried out their studies in 2D and 3D domains, concluding that the exclusion of a third dimension has a major impact on the prediction of CZ hydraulic behaviour.

Chen et al. [21] researched the impact of microbubble diameters ranging from 30 to 70 μm on the hydraulic behaviour of the DAF unit. Lundh's pilot tank was modelled as a 3D domain, discretized using 705.410 cells, whereby the authors simulated the flow for 1000 s (approximately twice the mean hydraulic residence time), modelling the free surface as a frictionless wall. For their part, Euler-Euler and Euler-Lagrange approaches were evaluated to ascertain which one would make a better prediction, with the result of the study being that the Euler-Euler approach gave a better prediction of experimental data. Finally, the influence of MB size on SZ hydraulics was evaluated, with authors reporting that larger bubbles were conducive to the formation of a stratified flow.

Rodrigues et al. [22] also modelled Lundh's pilot tank and studied the influence of 30, 50 and 70-μm bubbles on the stratified flow structure using the approach proposed by Chen et al. [21]. The 3D domain was discretized with 848.880 cells and simulated for two mean hydraulic residence times, and two multiphase approaches were evaluated, namely Euler-Euler and Mixture. Rodrigues et al. [18] compared their simulation with the results obtained by Chen et al. [21], even though the recycle rate and, in turn, the air quantity, is doubled in the case of Chen. The authors concluded that air concentration obtained using the Mixture model was higher in comparison to the Euler-Euler approach, that modelling of the free surface as a degassing boundary condition was

more realistic than the frictionless wall and that there was little difference in results when two different drag laws (applied to bubble movement) were used.

Most authors [21–24] carried out transient simulations with sufficiently small timesteps in comparison to mean hydraulic residence time. However, transient simulations are very time-consuming because long flow times are required to reach quasi-steady conditions, in which flow field variables remain almost constant over time. For this reason, other authors [20,27] carried out steady-state simulations, reporting acceptable agreement between the velocity field and experimental measurements.

Dissolved air flotation is a complex multiphase system that requires many computational resources in order to be properly solved. This work offers a novel concept and, most importantly, computationally affordable approaches that have been employed in the analysis of Lundh's pilot DAF tank. In order to predict air concentration and flow structure inside the SZ, two approaches were used, specifically, mono- and multi-diameter. The former considers one secondary phase with a unique bubble diameter, while the latter takes into consideration several secondary phases, each with a distinct diameter. It was ascertained that the results obtained by steady-state simulations were very similar to those obtained by sufficiently long flow-time transient simulations. Additionally, the solution obtained using the Mixture model was assessed as being practically identical to that obtained using Euler-Euler multiphase models. A novel concept termed critical bubble diameter was defined as the bubble size that equals bubble rising velocity and HL, with this diameter being used as a reference for selection of suitable bubble sizes for study purposes. An analysis was performed to evaluate, on the one hand, the impact of bubble sizes above and below the critical bubble diameter on the position of the WWL and, on the other, the effect of bubbles on the flow structure and on the air profile curves using the mono-diameter approach. Furthermore, a new multi-diameter approach was used to estimate the combined effect of different bubble diameters on the hydrodynamics of the SZ and to calculate bubble size distribution. The results obtained using the two approaches were compared to the experimental measurements taken by Lundh.

2. Materials and methods

Lundh's pilot tank [10] was analysed by means of CFD simulations. The whole separation system contained DAF unit, pre-treatment process and recycled circuit, although as the scope of this study was to analyse the DAF unit, the other system components were not included. The main dimensions of the tank are described in Fig. 1 (only half of the domain was simulated), and lines L1, L2 and L3, which correspond to 0.65, 1.05
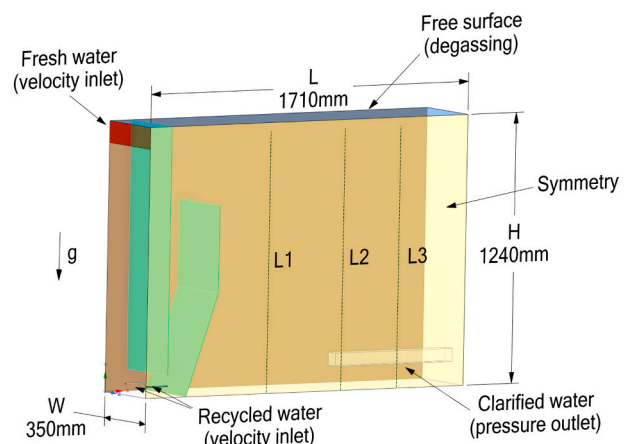

Fig. 1. Main dimensions of the pilot tank as well as boundary conditions used in the simulations. Lines L1, L2 and L3 correspond to the position of Lundh's measurements.

and 1.35 m of the x coordinate, can also be seen in the figure. Complete details of the tank geometry and configuration can be found in Lundh's PhD dissertation [6] or Rodrigues et al. [22].

Three different cases were analysed in this study (see detailed information in Table 1), and it was decided to retain Lundh's nomenclature, whereby the names of the cases were: M18, M19 and M21 [7]. The main part of the study was carried out using the M19 and M21 cases, although M18 was also researched.

The air flow rate and air fraction (see Table 1) were calculated based on the mean value of air concentration inside the CZ (C_{cz}) measured by Lundh. However, it should be pointed out that Lundh did not measure the diameter of the bubbles during his experiments, and this parameter is of major importance when performing CFD simulations. Hence, a range of diameters was researched in order to find which size would adjust better to the experimental data.

2.1. Mathematical modelling

Many authors [1,11,21,24,28] have used the Euler-Euler approach

Table 2
Rising velocity (V_b) and particle Reynolds number for different bubble sizes.

Bubble diameter (μm)	57	77	87	95	120
Stokes V_b (m/h)	6.36	11.6	14.81	17.7	28.17
Re_p	0.1	0.25	0.36	0.47	0.94

where ρ_q and ρ_p are primary (water) and secondary (air) phase densities, μ_q is the primary phase dynamic viscosity, $\overrightarrow{v}_{pq}$ is the relative velocity and d_p is the particle (bubble) diameter. For particles with $d_p < 120\ \mu m$, the particle Reynolds number will be smaller than unity (see Table 2). As all of the bubble diameters used in this study are smaller than 120 μm, the assumption of local equilibrium was met, with the continuity and momentum equations for the Mixture model taking the following form:

$$\frac{\partial \rho_m}{\partial t} + \nabla \left(\rho_m \overrightarrow{v}_m \right) = 0 \tag{3}$$

$$\frac{\partial \rho_m \overrightarrow{v}_m}{\partial t} + \nabla \bullet \left(\rho_m \overrightarrow{v}_m \overrightarrow{v}_m \right) = -\nabla p + \nabla \bullet \left[\mu_m \left(\nabla \overrightarrow{v}_m + \nabla \overrightarrow{v}_m^T \right) \right] + \rho_m \overrightarrow{g} - \nabla \bullet \left(\sum_{k=1}^{n} \alpha_k \rho_k \overrightarrow{v}_{dr,k} \overrightarrow{v}_{dr,k} \right) \tag{4}$$

[29] in order to predict flow behaviour in pilot and industrial DAF systems, reporting acceptable agreement with experimental data. Some of the research was carried out using the Euler-Lagrange approach [20,21]. However, Chen et al. [21] pointed out that the Euler-Euler approach showed an advantage in predicting air concentration in comparison to Euler-Lagrange [30]. Other authors [22,27,31] have reported good results with the Mixture model [32].

Two multiphase approaches were analysed in this study, namely, the Euler-Euler and Mixture models. Both models were found to provide very similar results (simulation results can be found in Appendix B) and, therefore, it is the Mixture model that is discussed in this section as it was used in the fundamental part of the study.

The Mixture model is a simplified multiphase model based on the Euler-Euler approach, and assumes that all phases behave as a mixture, solving only one set of momentum equations - that for the mixture. The slip of a dispersed phase relative to the continuous phase is calculated by balancing the drag and body forces resulting from density differences. The underlying assumption is that of a local equilibrium, in which the dispersed particles always move with their terminal velocity relative to the continuous phase. This means that bubbles are accelerated to their terminal velocity within a short distance, and a criterion for neglecting the acceleration is related to the relaxation time of a particle, τ_p. According to the Stokes regime, this is given by [32]:

$$\tau_p = \rho_p d_p^2 \Big/ 18 \mu_m \text{ for } Re_p < 1 \tag{1}$$

$$Re_p = \frac{\rho_q \left| \overrightarrow{v}_{pq} \right| d_p}{\mu_q} \tag{2}$$

where $\overrightarrow{v}_m = \left(\sum_{k=1}^{n} \alpha_k \rho_k \overrightarrow{v}_k \right) \Big/ \rho_m$ is the mass-averaged velocity, $\rho_m = \sum_{k=1}^{n} \alpha_k \rho_k$ is the mixture density, $\mu_m = \sum_{k=1}^{n} \alpha_k \mu_k$ is the mixture viscosity, α_k is the volume fraction of phase k, and n is the number of phases. Drift velocity $\overrightarrow{v}_{dr,k} = \overrightarrow{v}_k - \overrightarrow{v}_m$ is used to close the conservation equation and is related to relative (or slip) velocity $\overrightarrow{v}_{kq}$ via the following equation:

$$\overrightarrow{v}_{dr,k} = \overrightarrow{v}_{pq} - \sum_{k=1}^{n} c_k \overrightarrow{v}_{kq} \tag{5}$$

where $\overrightarrow{v}_{kq}$ is the velocity of phase k relative to phase q and $c_k = \alpha_k \rho_k / \rho_m$ is the mass fraction of phase k. In accordance with [32], the form of the relative velocity is given by:

$$\overrightarrow{v}_{pq} = \frac{\tau_p \left(\rho_p - \rho_m \right)}{F_{drag} \rho_p} \overrightarrow{a} - \overrightarrow{v}_t \tag{6}$$

where $\overrightarrow{a}$ is the secondary phase acceleration, $\overrightarrow{v}_t$ is the turbulence contribution to the velocity, and F_{drag} is the drag function.

Several drag laws were analysed, namely, Schiller-Naumann, Morsi-Alexander, Universal and Clift [33]. Very little difference was found between the drag coefficients for bubbles with diameter between 40 and 120 μm. Schiller-Naumann is a general-purpose drag law, and is therefore the one used in this study, while the drag function of the Eq. (6) is defined as follows: $F_{drag} = 1 + 0.15 Re_p^{0.687}$ (for $Re_p \leq 1000$).

The realizable k-ε model was used to deal with turbulence, with k-ε turbulence models having been thoroughly used in DAF system simulations [1,11,21,22,26,28,34]. These models consist of two empirically based equations for kinetic energy (k) and dissipation rate (ε). Park et al.

Table 1
Operating conditions used in this study. Recycled velocity inlet conditions required for CFD can be obtained from air and water flow rates.

Case	Fresh water (m³/h)	Recycled rate R (%)	Total water flow rate (m³/h)	V_s (m/h)	C_{cz} (ml/l)	Air flow rate (l/h)	Flow structure
M18	10	5	10.5	11.3	3	31.5	Semi-Stratified
M19	10	10	11	11.8	5	55	Stratified
M21	15	10	16.5	17.7	6	66	Stratified

[35] analysed different turbulent models in an industrial DAF unit and confirmed that the realizable k-ε model proved to make a better prediction. In addition, Bondelind et al. [20] have also used realizable k-ε model to simulate Lundh's DAF tank.

As regards boundary conditions, the pilot tank has a symmetry XY-plane that passes through a 0.35 m value of the z-axis; therefore, the symmetry condition was used to split the tank in two halves (see Fig. 1). The air mass sink term proposed by Ta [36] for the free surface was implemented via a user-defined function. Recycled flow injectors with 5 mm internal diameter (in the form of squares of equivalent area) were modelled as a velocity inlet, with the freshwater inlet being modelled as a velocity inlet with velocity value equal to 0.04 m/s (in the case of M18 and M19) and 0.06 m/s (in the case of M21). Turbulent intensity was set to 5% for both inlets, whereas clarified water outlet was modelled as a rectangular pipe (the same as [22,26]), with evenly distributed squares (20 squares per pipe) and in which a pressure outlet condition was set. A single-phase solution (within the multiphase framework, but with zero air flow rate) was previously calculated for each case and used as the initial solution for multiphase simulations.

The set of results presented and discussed in Section 3 were obtained by steady-state simulations, although transient simulations were also carried out. Bondelind et al. [20] put forward a theoretical argument that steady-state simulations could be used in DAF tank analysis, although as far as the authors are concerned, no practical demonstration has yet been published. A comparison was made between the transient approach taken by other authors [21,22] and the steady-state approach used in this study. The former authors provided the results they obtained after 1000 s of simulation flow time, which is equivalent to around two mean hydraulic residence (MHR) times. In our transient simulations, we reproduced their results at the aforementioned flow time but found that a quasi-steady solution was not obtained - at least not until a flow-time equal to six MHR times was reached. Moreover, the quasi-steady solution obtained proved to be very similar from a qualitative and quantitative point of view to the solution obtained by steady-state simulation. The results and discussion of this benchmark study can be found in Appendix A.

2.2. Mesh used for simulations

Firstly, a mesh of 0.85 million cells was built, similar to that done by other authors [21,22]. This mesh was used to carry out transient simulations (see Appendix A), although when refined, it was found that the steady-state solution changed while the number of cell elements increased. Therefore, it was decided to perform a mesh independency test in order to determine the discretization error and obtain sufficiently fine mesh.
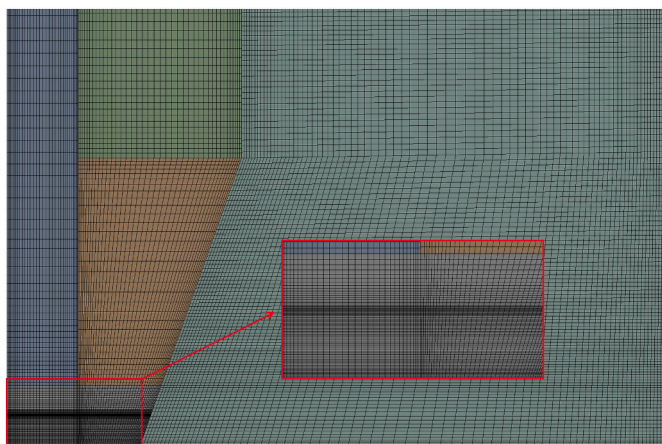

Fig. 2. Hexahedral high-quality mesh of 5.7 million cells. The injection region was refined in order to capture jet spreading.

A procedure for estimating the discretization error based on Richardson Extrapolation was proposed by Celik et al. [37]. Currently, this is the most practical method available for estimation of numerical uncertainties. Three meshes, with high quality hexahedral elements (a mesh example can be seen in Fig. 2), were refined systematically starting from a coarse mesh, which contained 2.8 million elements. A refinement factor of around 1.25 was used in order to generate medium-size and fine-size meshes, resulting in medium and fine meshes with 5.7 and 10.7 million elements being created.

In order to perform mesh analysis, it is necessary to select a flow variable φ, which is a key parameter for the study in question. In this study, the volume-weighted average of air fraction in the whole tank was chosen. The grid convergence index (or GCI) represents an upper limit of the discretization error and is calculated from the estimated relative error multiplied by the safety factor (1.25 for three-mesh study, see [37]).

The Euler-Euler approach was used to analyse the M18 case with 67 μm bubbles in a steady-state simulation. In order to secure a small iterative error, R_{air}(Eq. (7)) was maintained below 10^{-5} in the simulations with the three meshes. Calculated GCI for the fine mesh was equal to 1.1%, although simulating a ten-million-cell mesh proved unpractical due to the high computational burden. On the other hand, the use of coarse mesh may have significantly affected the accuracy of the results. Hence, in this study, the 5.7-million mesh was used in order not to lose accuracy and not to dramatically increase calculation time. The value of GCI_{medium} was equal to 4.7%, and this uncertainty value was therefore assumed in the results.

In this study, it has been shown that the number of elements required for a mesh independent solution is considerably higher than that employed by other authors in literature. Hence, it is recommended that a mesh independence analysis be performed in order to quantify the discretization error in DAF tank studies.

2.3. Numerical resolution of the mathematical model

The mathematical model was solved using the finite volume method (FVM). All of the terms of the partial differential equations were discretized using second order schemes, except for the convective term of the volume fraction equation that was discretized using a first order upwind scheme. Pressure, velocity and volume fraction of the phases were solved in a coupled way, with commercial ANSYS Fluent 2020R1 software having been used to solve the previously proposed mathematical model. All the simulations were performed in parallel mode with 2.3 GHz*64 CPUs on a Linux server (Intel Xeon Gold 5218, 256 GB RAM), with average time required to perform a steady-state simulation using the Mixture model being around 24 h using the mono-diameter approach and 48–120 h in the case of the multi-diameter approach (depending on the number of secondary phases).

The convergence criteria were carefully analysed, with continuity, velocity and turbulence residuals being maintained at values below 10^{-5} except for air fraction, whose residual was slightly higher. In order to accept the solution, all the flow variables had to reach a stable value, and in steady-state simulations, one additional criterion was imposed in order to control air fraction convergence:

$$R_{air} = \frac{Abs[m(n) - m(n - Np)]}{m(n)} \qquad (7)$$

where $m(n)$ is the volume-weighted average of air fraction, n is the current iteration and Np is the number of iterations to be considered (in this case Np was equal to 50). R_{air} was maintained below 10^{-5} for mono-diameter analysis and below 10^{-4} for multi-diameter analysis. In the case of the latter, this criterion was imposed for every secondary phase, and by applying this rule, we ensured that all simulations had a very low iterative error.
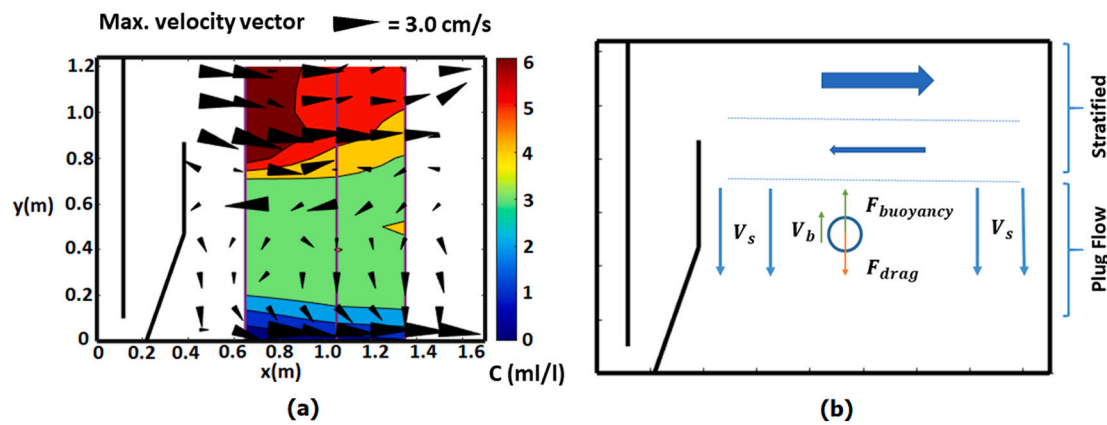
Fig. 3. Lundh's contour of air concentration together with velocity vectors, recreated in the case of M21 (a). Simplified stratified structure scheme (b).

2.4. Bubble size: critical diameter concept

If realistic CFD results were to be obtained and used for design and operation, it would be necessary to know the bubble size distribution (BSD) that exists in the DAF tank analysed. The problem is that bubble size is difficult to measure in existing systems or to predict in the systems that are to be designed. Lundh did not measure bubble diameter and for this reason, the CFD studies that were carried out on his pilot plant used different bubble sizes. For their part, Bondelind et al. [20] used 40, 80 and 120 μm, Chen et al. [21] used 30, 40, 50, 60 and 70 μm, Rodrigues et al. [22] used 30, 50 and 70 μm and Deng et al. [24] used 40, 80 and 120 μm. The flow structures obtained in previous CFD studies of the Lundh pilot plant were especially dependent on bubble diameter, and so for this reason, other authors (Emmanouil et al. [28]) have also analysed the effect of the different bubble diameters in a different DAF system.

In order to determine suitable bubble sizes for the CFD analysis of the present study, the water velocity vectors and air content profile curves reported by Lundh et al. [7] were analysed together. Fig. 3a shows the contour of air content and water velocity (plotted as cones) that were recreated from Lundh's data (see also Fig. 5a). It should be pointed out that during Lundh's experiments, air profiles and water velocity vectors were measured with several months' difference [6], meaning that there may be a discrepancy between air concentration and velocity vector fields. Nevertheless, this difference is assumed not to be important and the combined contour (air profile+vectors) provides reliable information for analytical purposes. Fig. 3a shows two clearly identified flow structures. In the upper part, the stratified flow is represented by a horizontal flow, rich with bubbles, which is moving in the direction of the far end wall. In the lower part of the SZ, air content is lower, and the flow is moving vertically in the direction of the outlet pipe, forming a plug-flow-like structure. This vertical flow drags air bubbles up to the level of the outlet, with the WWL being located at that height (around 0.1 m). As a conclusion, it can be said that the WWL does not necessarily have to divide the stratified flow from the plug-flow structures.

In order to reproduce the structure reported by Lundh, some of the bubbles must be dragged by the plug flow, in which case their rising speed (V_b) will be lower than the downward velocity of the vertical flow (V_s, same as HL). Consequently, critical diameter (D_c) is defined as the bubble size where V_b is equal to V_s. It should be noted that V_b is obtained as a result of buoyancy and the drag force equilibrium (see the simplified scheme in Fig. 3b).

From a pragmatic point of view, Stokes's law was used to calculate the D_c, although it should be pointed out that this is an approximate value of the critical diameter because turbulence contribution was not included. However, as the turbulence level in the lower part of the SZ is low, there should be no major change in diameter. In cases M18 (HL = 11.3 m/h) and M19 (HL = 11.8 m/h), bubble D_c is around 77 μm (see Table 2). Four different bubble sizes were selected for the analysis, in the

Table 3
Volume-weighted average of air concentration (AAC), white water level position (WWL), air in the mass sink term in comparison to entering air (degassing air) and bubble removal efficiency defined as hydraulic loading divided by MB rising velocity (MB Removal eff.) in the cases of M18, M19 and M21.

M18	57 μm	67 μm	77 μm	87 μm
AAC (ml/l)	2.02	1.86	1.31	0.48
WWL (m)	0.1	0.1	0.3	0.89
Degassing Air	71%	87%	100%	100%
MB Removal eff.	56%	78%	100%	100%
M19	57 μm	67 μm	77 μm	87 μm
AAC (ml/l)	3.46	3.19	2.87	0.97
WWL (m)	0.1	0.1	0.14	0.89
Degassing Air	68%	83%	99%	99%
MB Removal eff.	54%	74%	98%	100%
M21	85 μm	90 μm	95 μm	100 μm
AAC (ml/l)	4.13	3.84	1.75	1.39
WWL (m)	0.1	0.13	0.73	0.89
Degassing Air	92%	99%	100%	100%
MB Removal eff.	80%	89%	99%	100%

course of which critical diameter and sizes above and below this were researched, namely 57, 67 and 87 μm. In case M21 (HL = 17.7 m/h), critical diameter was 95 μm and sizes selected for the analysis were 85, 90, 95 and 100 μm.

With the aid of CFD simulations, it was noted that using air bubble sizes greater or less than D_c significantly affects the air content, flow structure and WWL position inside the SZ (see Table 3 in the results and discussion section). It is expected that all bubble sizes greater than D_c will tend to form a layer of air closer to the free surface, while bubbles that are lower than D_c will fill the SZ domain up to the level of the outlet pipe.

Finally, it should be pointed out that mechanisms involving any change in size of bubbles are not implemented in this study. Information exists in literature about the coalescence and break up phenomenon in flotation columns [38–41]. However, the bubble diameter used in the flotation column (around 1 mm) is considerably larger than microbubbles in the DAF and the use of these models in dissolved air flotation needs to be properly validated. Rodrigues et al. [42] researched into Lundh's pilot tank using a population balance model with coalescence and break up models that were validated in flotation columns, obtaining little agreement between simulation results and experimental data.

2.5. Multi-diameter approach

In this section, a new approach to analysing hydraulic behaviour of

the separation zone is presented. A wide range of bubble sizes can be found in DAF tanks and modelling of the continuous BSD remains a challenging process. However, instead of directly introducing the continuous BSD and mechanisms that affect distribution, several secondary phases are included in the mixture model, each individual phase having its own distinct diameter. The critical diameter concept is used to select representative bubble diameters, whereby 82 and 87 μm diameters were selected for the M19 case analysis as bubble sizes above D_c and 57 μm as the size below D_c. Moreover, 77 μm was added to see the effect of the bubbles with the size being very close to the critical diameter.

This approach not only permits different bubble dynamics to be taken into account, but also the computational effort is not prohibitively costly. The key advantage of this approach is that interactions between several air phases and the carrier phase can be analysed, and it also allows the Sauter diameter of the bubbles to be calculated throughout the DAF tank.

Computational cost is relatively low in comparison to the Euler-Euler approach, although the maximum number of secondary phases remains a constraint. On the one hand, computational cost is increasing and on the other, convergence difficulty rises with the addition of every secondary phase.

Simulations with multiple secondary phases have already been carried out by Bondelind et al. [20] and Emmanouil et al. [28]. However, these authors employed a Euler-Lagrange approach in simplified 2D models and did not conduct an in-depth analysis of the effect of the combination of the three secondary phases on SZ hydraulics. Moreover, the Euler-Lagrange approach is limited by the fact that bubble size distribution cannot be obtained directly.

3. Results and discussion

In this section, the results of Lundh's pilot tank simulations are presented, in the course of which the influence of microbubble diameter (MB) on the hydraulics of the separation zone was studied. Additionally, the importance of the critical diameter on the bubble's presence in the domain is also analysed, and finally, the multi-diameter approach is used to predict air distribution in the stratified flow structure. The CFD results obtained were compared to air concentration profiles and water velocity vectors contours that were measured by Lundh. These magnitudes are the most representative and were also used to validate CFD results by other authors [20–22,26,31].

3.1. Analysis of mono-diameter bubbles on the hydraulic behaviour of the separation zone

The influence of bubble diameter on the flow pattern is analysed in the case of M19 first (see Table 1). The results were plotted in a similar way to make the comparison between Lundh's experimental data (Figs. 3a and 5a) and CFD simulations easier. In his work [6], Lundh warned that the velocity vector module measured might contain a major error due to the intrinsic difficulty of using Acoustic Doppler Velocimetry (ADV) in this complex multiphase flow. For this reason, only the maximum velocity value is shown in the images.

Simulations carried out with 57 and 67-μm diameter showed a breakthrough-like pattern inside the SZ (see Fig. 4), although this phenomenon was not observed in Lundh's experiments (see Fig. 5a). After passing beyond the baffle wall, water current then moves in the direction of the outlet pipe. However, following analysis of the other XY planes, it was observed that, further away from the air injection device, the effect of the break-through-like pattern was less pronounced. Flow behaviour is
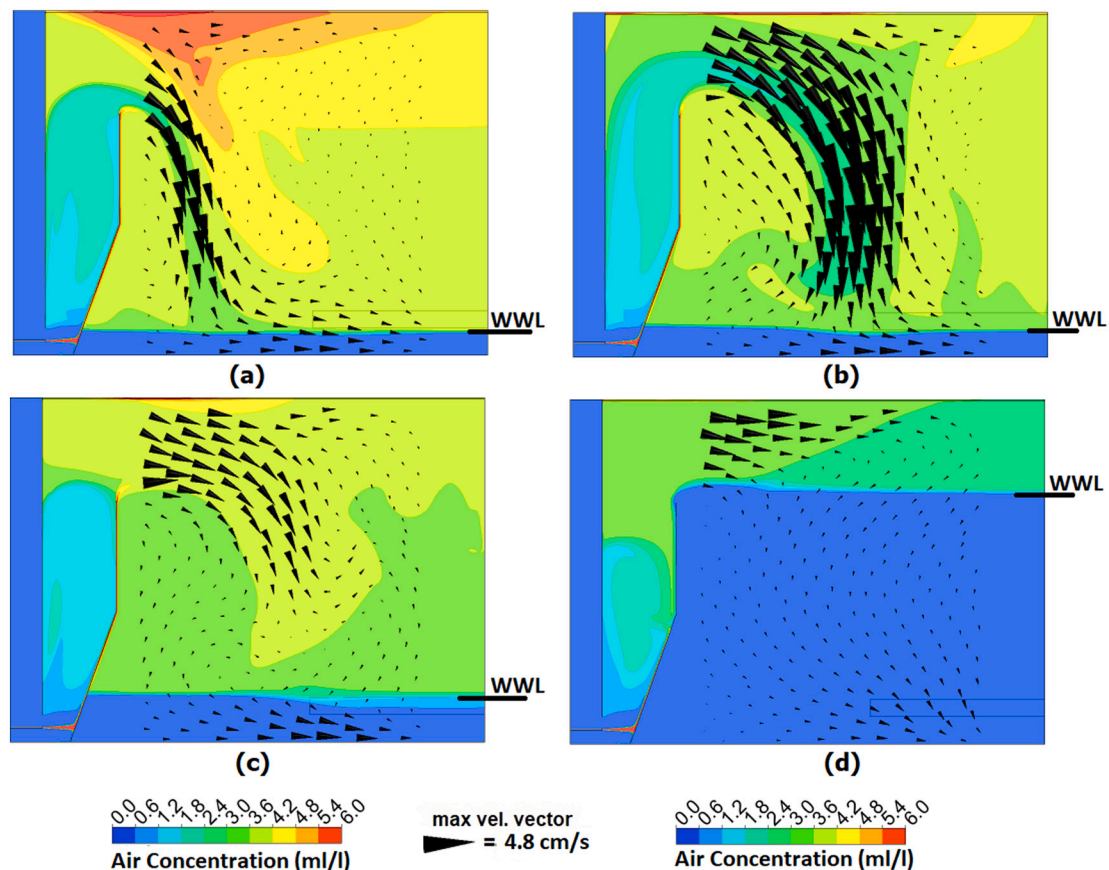

Fig. 4. M19 air concentration contour along with water velocity vectors for different microbubbles: 57 μm (a), 67 μm (b), 77 μm (c), 87 μm (d).
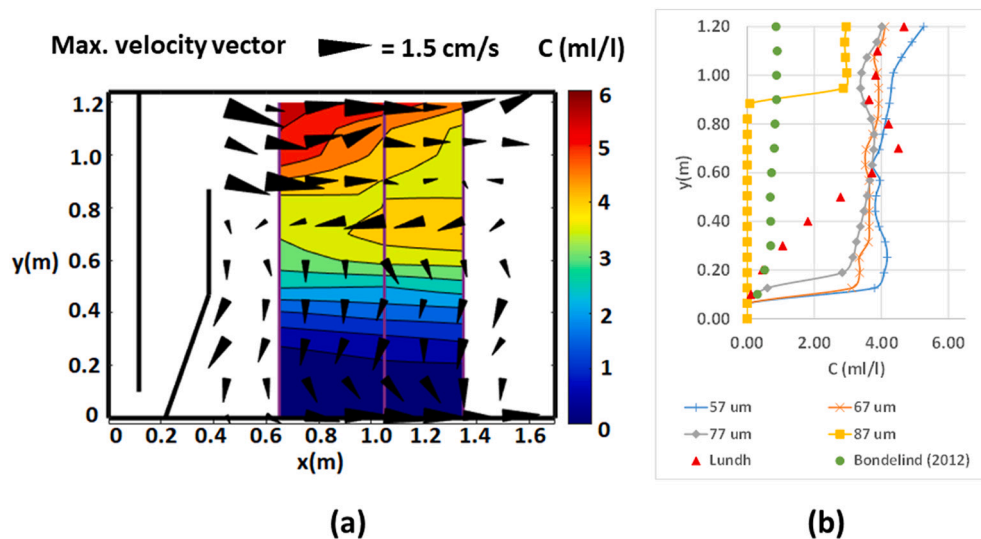
Fig. 5. Lundh's contour of air concentration together with velocity vectors, recreated in the case of M19 from lines L1, L2 and L3 (a). Air-content profile along line L1 for bubble diameter 57, 67, 77 and 87 μm(b); Results from Bondelind et al. (2012) for 80 μm bubbles were also added.

different in the case of 87-μm diameter bubbles. This MB size is greater than critical diameter ($\approx$77 μm) and, as a result, most of the air escapes across the degassing condition and WWL is located above the tip of the baffle (see Fig. 4d). Density is higher below the WWL, whereby the flow current filled with bubbles cannot penetrate deeper into the SZ. Consequently, the flow is forced to move towards the opposite wall. Additionally, higher water velocity values close to the free surface were observed for 87 μm diameter bubbles (similar to Lundh's Fig. 5a), although air concentration was not well predicted. Finally, the 77-μm is a very sensitive diameter, and the flow develops behaviour somewhere between 67 and 87 μm.

Air distribution along lines L1, L2 and L3 can be seen in Figs. 5b and 6a-b, and all the simulations with mono-sized bubbles predicted air concentration around 4 ml/l above the WWL. This fact is represented by almost vertical-shape curves in the figure, while in contrast, below WWL air concentration drastically falls to values close to zero. The results of Bondelind et al. [26] for 80 μm bubbles were included for comparison in Figs. 5b and 6a-b, in which it can be observed that the air quantity predicted using the Euler-Lagrange approach is considerably lower than experimental data and that predicted using the Euler-Euler approach.

It was also observed that bubble diameter had a major effect on the position of the WWL and, as a result, the total quantity of air in the SZ. Rising velocity of the bubbles with 57, 67 and 77 μm diameter was lower than HL (see Table 2) and, as a result, WWL penetrates deeper into the tank up to outlet pipe level (located 10 cm above the ground). The results obtained from the simulations with MB diameter of 57 μm (see Figs. 5b and 6a-b) showed acceptable results of between 60 and 120 cm in comparison to experimental data [7], although it was not possible to reproduce the gradual reduction in air content below 60 cm with mono-diameter bubbles.

Case M21 was studied in accordance with a mono-diameter approach, whereby the flow rate was increased by 50% (in terms of M19), as a result obtaining HL equal to 17.7 m/h (see M21 in Table 1). Four bubble sizes were selected for the analysis including critical diameter, which was around 95 μm. The major changes in WWL and air concentration would be expected to be seen in the size range between 90 and 100 μm.

The air contour along with the velocity vector in the case of M21 can be seen in Fig. 7. The clear difference should be pointed out between the behaviour of the air bubbles, whose size was less than critical diameter (Fig. 7a-b) and greater than critical value (Fig. 7d). MBs with 85 and 90-μm diameter occupied almost the whole separation zone to outlet pipe

level. In addition, the main water current moved in the direction of the far end wall in the upper part and was then deflected back to the baffle in the lower part. The same pattern was also observed on the other XY planes, indicating that the effect of the third dimension is less pronounced than in the case of M19. Similar behaviour was reported by Lundh [7] as stratified flow. It is worth noting that, qualitatively, 90 μm bubbles (Fig. 7b) showed very similar air and velocity fields in comparison to experimental data (see Fig. 3a), while in the case of the 100-μm bubble (Fig. 7b), behaviour was completely different in comparison to 85 and 90, although it was similar to 87-μm bubbles in the case of M19 (Fig. 4d). The air phase was concentrated in the upper part and most of the bubbles were not capable of passing to the lower part due to high density difference. In the case of 95 and 100 μm MBs, the plug-flow-like pattern was observed below the WWL.

Air concentration profiles plotted along lines L2 and L3 can be seen in Fig. 6c-d. The results showed that in the case of 85 and 90 μm bubbles, WWL was positioned around 10 cm above the bottom of the tank, at outlet pipe level, while in that of 100 μm bubbles, WWL was located at the height of 87 cm above the ground. Air concentration profiles for 90-μm bubbles, measured on lines L2 and L3, proved to be more in line with experimental data, in comparison to 100 μm. It is likely that mean bubble diameter in Lundh's experiment was lower than 95 μm, because the position of the WWL as observed in the experiment was located around outlet pipe level (see Fig. 6c-d).

A summary of the mono-diameter simulations can be seen in Table 3. It is worth noting that there was a major difference in volume weighted average of air concentration between the lowest and highest bubble diameter value researched in each case. Air concentration decreased to a major extent when MB diameter was greater than critical diameter. In addition, the position of the WWL was also especially sensitive to critical diameter, meaning that small changes in HL might significantly affect the WWL in CFD simulations. This fact can be observed in Table 3 when comparing values of the WWL position of 77-μm bubbles in M18 and M19 simulation results. In the case of M18, the HL is slightly lower, and therefore the WWL position is slightly higher (0.3 m) in comparison to M19 (0.14 m).

Finally, it should be added that M18 contours were not included in this paper; however, the conclusions drawn in the case of M18 were very similar as for M19, and only air phase-related values can be seen in Table 3. Air eliminated by means of the mass sink term divided by air entering through the recycled inlets (Degassing air in Table 3) was compared to air bubble removal efficiency used in conventional DAF
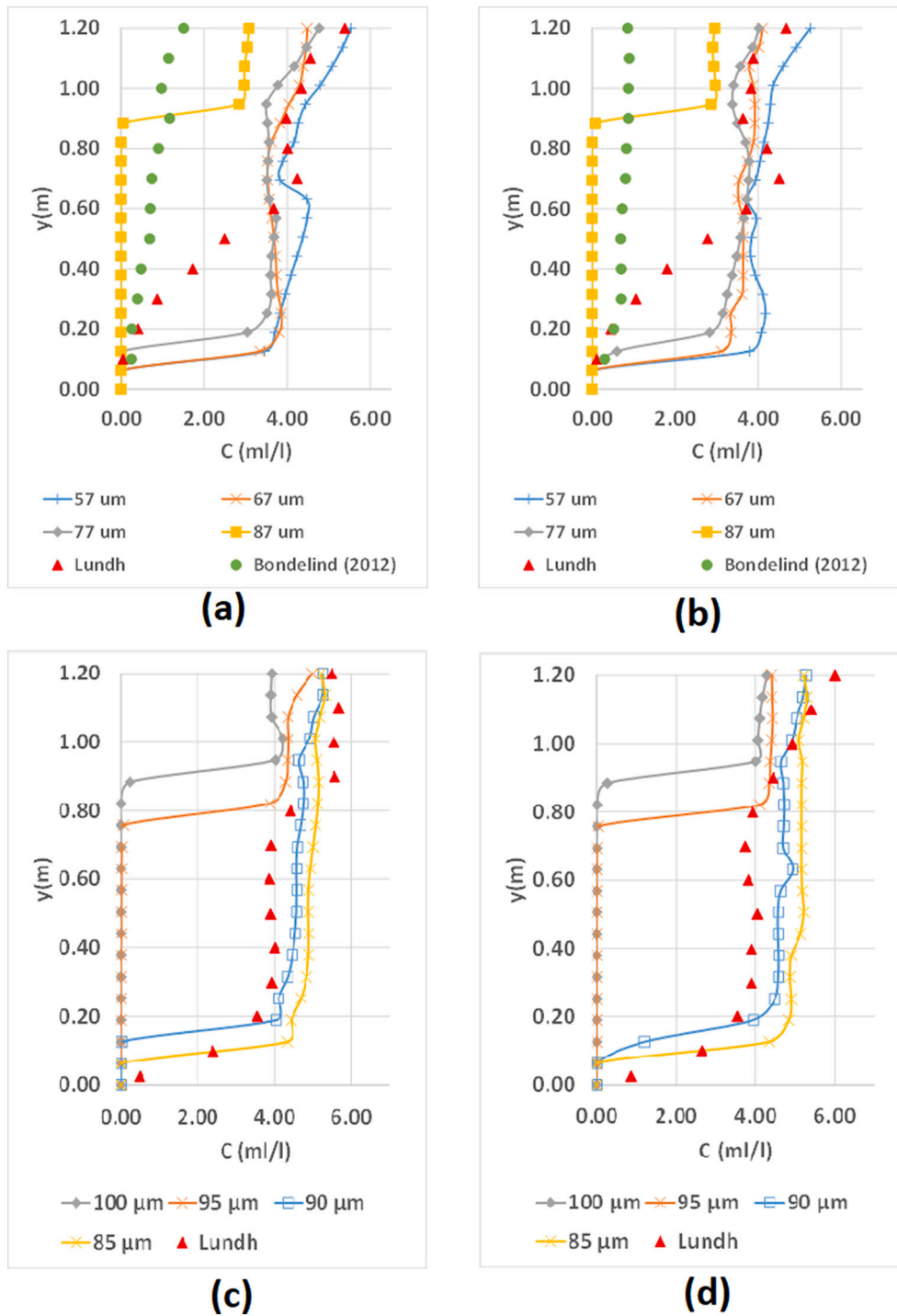
Fig. 6. A comparison of air-content profiles on the y-axis for different microbubble diameters 57, 67, 77 and 87 μm. L2 (a) and L3 (b) in the case of M19 (results from Bondelind et al. (2012) for 80 μm bubbles were also added); Air-content profiles for 85, 90, 95 and 100 μm in the case of M21, L2 (c) and L3 (d).

designs (V_b/V_s). A discrepancy was found in the case of MB diameters that were lower than critical, which could be explained by the fact that conventional theory only takes into account air leaving above the SZ domain and that the CFD also considers air leaving above the CZ.

3.2. Multi-diameter analysis

In the previous section, it was seen that single-diameter bubbles created even distribution of air inside the SZ up to outlet level, namely, around 4 ml/l of air concentration in the case of M19 and M21.

Nevertheless, experimental results obtained from the M19 case showed a gradual decrease in air concentration below 60 cm of tank height, although this behaviour was not possible to predict with single diameter bubbles. In the case of M21, the experiments did not detect any progressive decay of air concentration, and so the prediction made using the mono-diameter was sufficient.

A simulation with operating conditions as in the M19 case was carried out using the multi-diameter approach. As mentioned in Section 2.5, four secondary phases were included with 57, 77, 82 and 87 μm bubble diameters. The same total quantity of air as in the mono-diameter
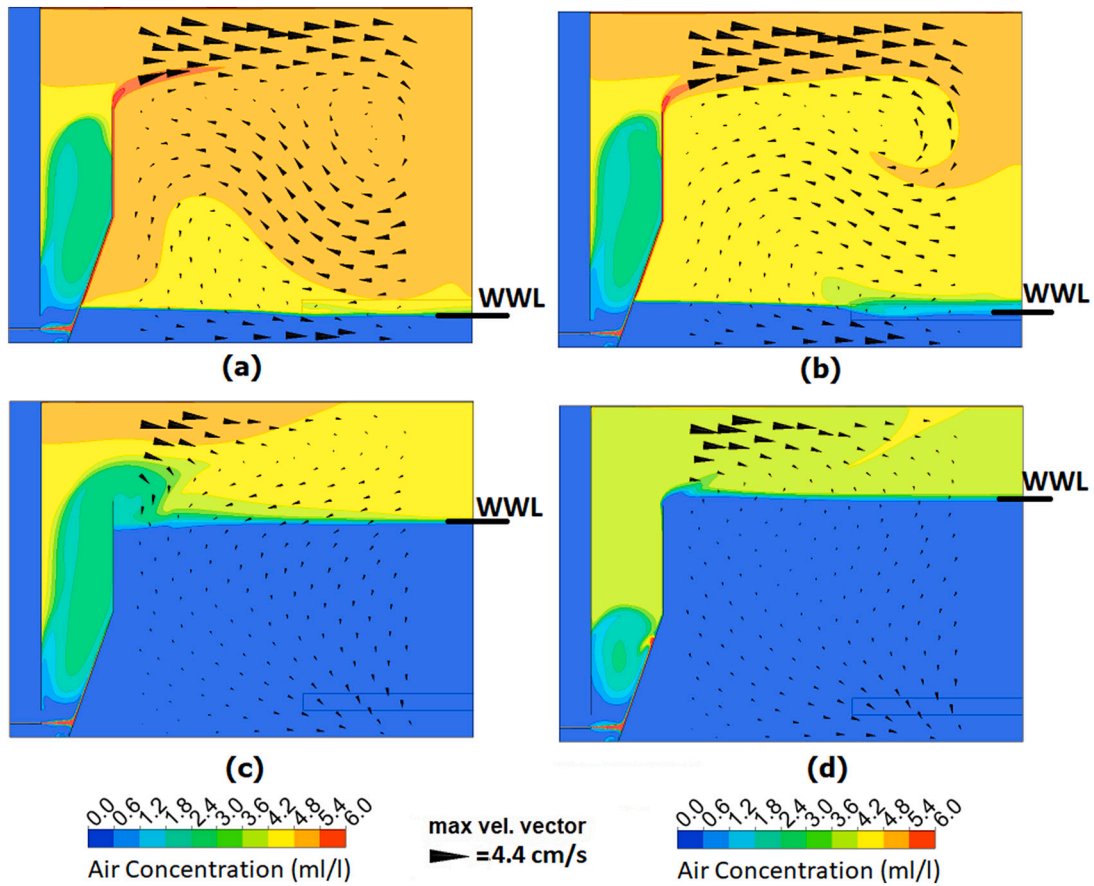
Fig. 7. M21 air concentration contour along with water velocity vectors for different microbubbles: 85 μm (a), 90 μm (b), 95 μm (c), 100 μm (d).
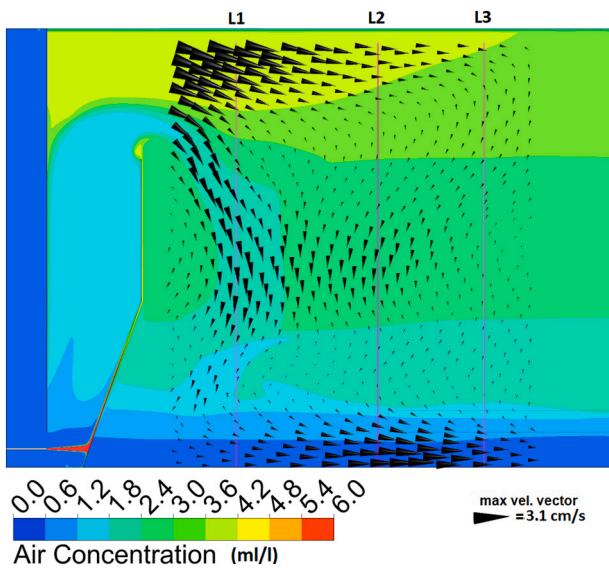

Fig. 8. Air concentration contour formed as a combination of the four secondary phases along with water velocity vectors in the case of M19.

approach was introduced at the recycled velocity inlet and the air was evenly distributed across the four phases.

Stratified flow structure was obtained by combining bubbles with different rising velocities (see Fig. 8). Air concentration was higher in the upper part of the SZ because MB of a greater size occupied the region closer to the free surface, while smaller MBs filled the whole SZ domain

up to outlet pipe level (see Fig. 10a). For its part, air contour evidenced different concentrations that were reduced as the y coordinate decreased, especially in the region of the L2 and L3 lines.

Regarding velocity vectors, higher velocities were observed close to the free surface, on the upper part. The main current moved from the CZ to SZ in the direction of the opposite wall and the current was then deflected downward. However, a small proportion of the main flow formed a break-through-like pattern in the region closer to the separation baffle. Finally, the plug-flow structure formed in the lower part. Higher velocities on the upper part and plug-flow on the lower part are a phenomenon reported by Lundh (see Fig. 5a), although a break-through-like pattern and higher velocities at the top were also observed in mono-diameter results in the case of 57 and 87 μm (see Fig. 4a and d), meaning that the multi-diameter simulation maintains the characteristics of the mono-diameter ones. Following analysis of the other XY planes, it was observed that the break-through-like pattern is less pronounced further away from the injector and, as a result, the plug-flow-like structure extends through the whole length of the separation zone below the tip of the baffle.

Air content profiles, measured on lines L1, L2 and L3, can be seen in Fig. 9a-c. Air concentration was better predicted compared to experimental results in the region of the L2 and L3 lines because of lower water velocity. In comparison to mono-diameter simulation of 57 and 87 μm MBs, the results obtained using the multi-diameter simulation were able to predict a progressive reduction in air content below 0.6 m of the y coordinate. Nevertheless, air concentration predicted in the region from 0.6 to 1.2 m was lower than values reported by Lundh. Finally, there was less agreement with experimental data in the case of the L1 region, where the short-circuit pattern was detected.

Fig. 10 shows air distribution inside the SZ, while a histogram of air diameter distribution along line L2 can be seen in Fig. 10a. As rising
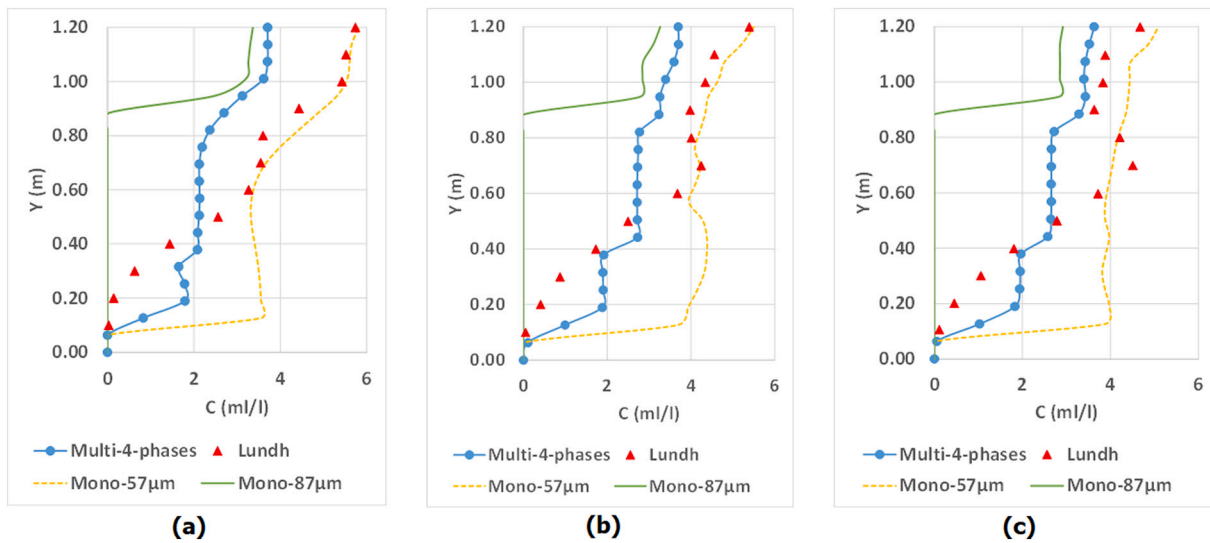
Fig. 9. A comparison of air content profiles on the y-axis. Lines L1 (a), L2 (b) and L3 (c) in the case of M19 simulated with four secondary phases. Air profiles from 57 and 87 μm MB using the mono-diameter approach in the case of M19 were included for comparison.
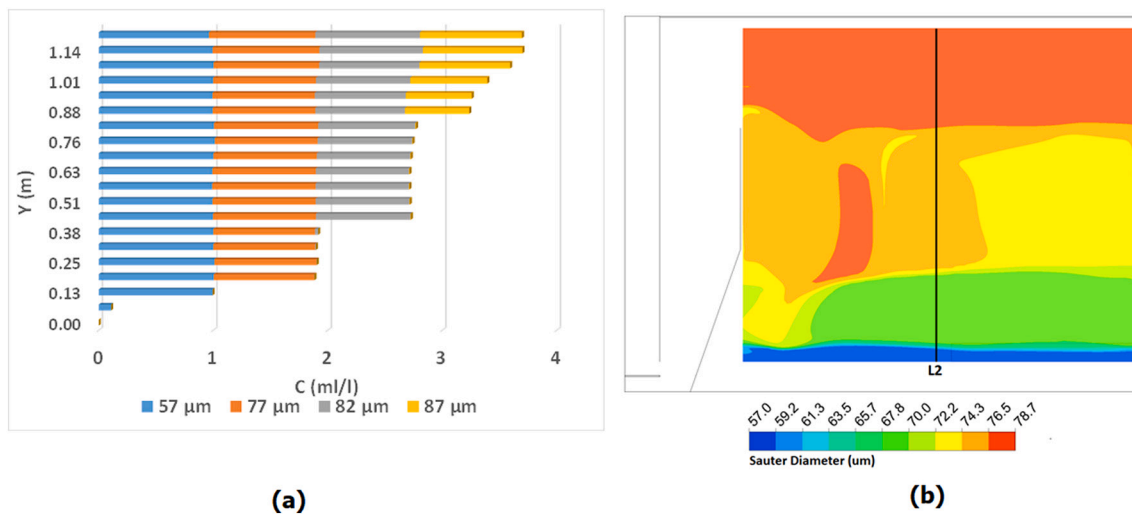

Fig. 10. Air phase histogram measured on line L2 (a); Contour of Sauter Diameter in the case of M19 (b).

velocity of 57-μm bubbles was well below HL, their presence could be found in the whole separation zone above the outlet pipe. Conversely, in the case of 87- μm bubbles, rising velocity was higher than HL. As a result, their position was limited to a 30-cm-high layer, located below the water surface (see similar behaviour in mono-diameter simulations in Figs. 4d and 7d). Intermediate sizes (77 and 82 μm) were distributed in different heights as a function of their rising speed.

The Sauter diameter contour was created by combining air distribution of the four secondary phases (see Fig. 10b). This contour indicates that most of the large bubble diameters were concentrated on the top layer, although a small part of the 82 and 87 μm bubbles were dragged deeper into the SZ domain due to the break-through current. As a result, the Sauter diameter value increased in the region of the L1 line, although conversely, uniform decay of the bubble Sauter diameter was observed closer to the opposite wall. Ultimately, the results showed that air distribution contains characteristics of the four secondary phases. This observation was also reported by Bondelind [20].

Finally, in order to assess the sensitivity of the model in terms of air distribution, a couple of additional studies were undertaken, such as changing air concentration of the highest and lowest bubble diameters. This means that the original air distribution (see Fig. 9a-c), which

comprised evenly distributed air concentrations, was modified. The volume fraction of 87 μm air bubbles was doubled and total air quantity at the recycled inlet was therefore increased by 25% in comparison to the air concentration value measured by Lundh. An equivalent experiment was conducted using the 57 μm fraction, where only the 57-μm fraction was modified, and the rest remained equal.

When 87 μm air fraction was increased, the tendency was to move the upper part (between 0.8 and 1.2 cm) of the curve to the right, i.e. by increasing air concentration only on the top most layer (see Fig. 11). In contrast, when the 57-μm fraction was increased, all of the air profile was displaced to the right, meaning that total presence of air increased in the domain. In summary, these studies showed that it is possible to modify the shape of the air profile obtained by varying air fraction distribution and bubble diameter.

4. Conclusions

The CFD model of Lundh's pilot tank was analysed using mono and multi-diameter approaches, in the course of which it was ascertained that the solution obtained via a steady-state simulation was very similar to that obtained by sufficiently long flow-time transient simulations.
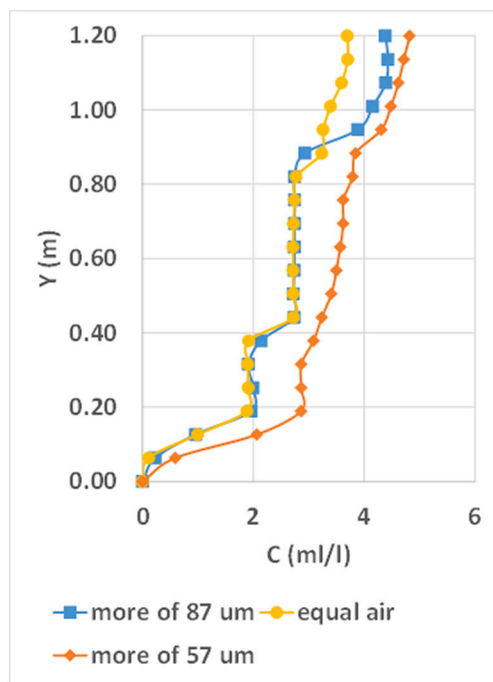
Fig. 11. Air content profile on the y-axis for line L2 (x = 1.05 m). Original air concentration was compared to air distribution where more 57 μm or 87 μm bubbles were added.

Additionally, it was confirmed that the multiphase Mixture model offered almost identical results to the Euler-Euler model and is suitable for carrying out DAF tank simulations.

The critical diameter (D_c) concept was introduced and demonstrated that it is a useful tool for DAF CFD studies. For all of the case studies examined, the results obtained from the mono-diameter simulations showed two clearly discernible types of behaviour, depending on whether the bubble diameter was greater or less than D_c. In simulations where the selected size was greater than D_c, bubbles would be concentrated in the upper part of the SZ. As a result, the density of the layer located closer to the free surface was lower, forcing the water current to move in the direction of the far end wall. Water velocity vectors were similar to experimental results although air profile curve was not predicted. In the case of simulations in which the bubble size was less than D_c, the whole SZ was filled with air up to outlet pipe level. In all mono-diameter simulations, air profile plots were shown as almost vertical

curves up to white water level (WWL).

The experimental results, in which Lundh obtained a smooth air profile curve with progressive decrease below 60 cm of SZ height (M19 case), were not possible to reproduce using the mono-diameter approach. Nevertheless, the approximately uniform air distribution (up to outlet pipe level) predicted in the case of M21 was closely in line with experimental data. In order to reproduce a smooth air profile curve, the combined effect of different bubble sizes close to the critical diameter value proved necessary.

The multi-diameter approach is proposed as an appropriate method for predicting the gradual reduction of air reported by Lundh in the case of M19. A stratified flow structure was reproduced, although a small, short-circuit-like pattern was formed close to the baffle. The results showed that air bubbles were distributed in layers as a function of their rising speed, generating an air profile curve very similar to the curve reported by Lundh. For its part, prediction considerably improved for tank height lower than 60 cm, although in contrast, prediction of air concentration worsened closer to the free surface. Additionally, this approach provided the chance to analyse air distribution and calculate the mean values of the bubble diameter as a function of tank height.

Sensitivity of the model to changes in air distribution in the inlet was evaluated, its being observed that increasing the quantity of the air phase of the highest diameter affected only the upper layer of the SZ. Meanwhile, an increase in the fraction of the lowest diameter displaced the air profile curve to the right, meaning that air concentration increased in the whole SZ up to outlet level.

This CFD study was conducted on a pilot DAF tank, although the approaches and ideas proposed in this study are equally valid for a full-scale tank analysis. They can be used by designers in the preliminary design of the SZ, in cases where bubble sizes are not known. In addition, CFD modellers in the wastewater field can also benefit from them to improve prediction of their simulations.

Declaration of competing interest

The authors declare that they have no known competing financial interests or personal relationships that could have appeared to influence the work reported in this paper.

Acknowledgements

Appendix A. Benchmark using the studies by Chen et al. and Rodrigues et al.

Chen et al. [21] carried out simulations in Lundh's DAF tank using 0.01 s timesteps and reported a converged solution for a flow time of 1000 s, which is approximately two mean hydraulic residence times (MHR ≈ 490 s). Additionally, Rodrigues et al. [22] and Deng et al. [24] also obtained their results simulating up to a flow time of 1000 s.

Our intention was to reproduce the studies by Chen and Rodrigues and carry out transient simulations of M18 and M19 cases using the Euler-Euler approach. The domain was discretized with 0.85 million cells, which is a mesh similar in size to that used by Chen and Rodrigues. Chen reported close agreement with experimental data for 50 and 60 μm bubble sizes, and so 50 μm diameter bubbles were therefore selected to analyse the M18 and M19 cases.

Case study M19 was simulated in accordance with the methodology proposed by Chen et al. [21]. The boundary conditions were the same as those reported by the authors, with the most significant being that the water surface was modelled as a frictionless wall. The air profile on line L2, obtained for different flow times, can be seen in Fig. A1 (a), while air profile values for 1000 s were taken from Chen and included in the figure. The results showed that if the simulation was stopped at 1000 s, the air profile obtained would be closely in line with experimental data provided by Lundh et al. [7]. However, if the simulation was continued up to 3000 s, the air concentration curve would take the form of an almost vertical line, this indicating that the air phase tends to be evenly distributed throughout the whole SZ above the outlet pipe, with concentration value around 4 ml/l. Ultimately, it was observed that the volume-weighted average of air fraction in 3000 s was increased by 51% in comparison to 1000 s. Therefore, two MHR times proved not to be enough to obtain a stable solution for the M19 case study. It is worth mentioning that in this study, a quasi-steady solution was not possible to obtain due to convergence difficulties that appeared after 3000 s. Since the free surface was modelled as a frictionless wall, an accumulation

of air appeared adjacent to the free surface that prevented the simulation from converging.
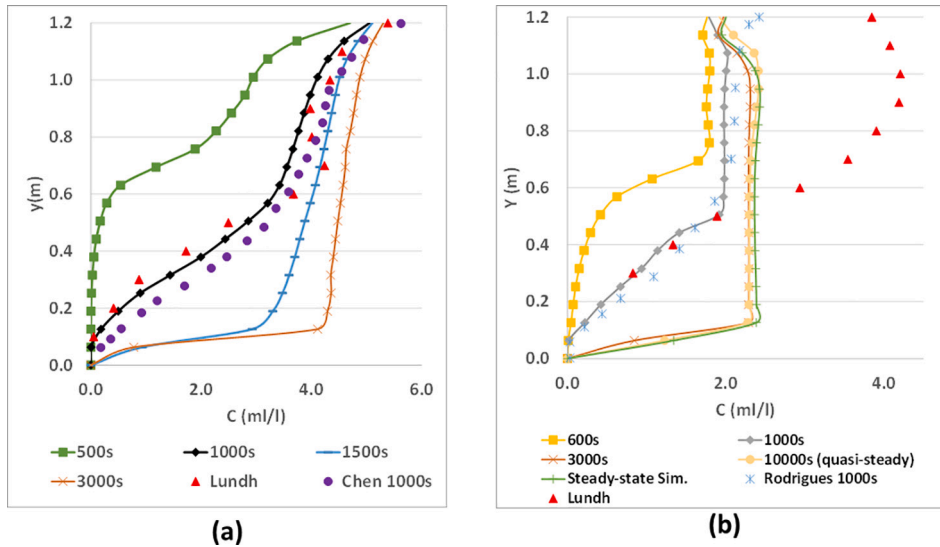

Fig. A1. Air concentration profile on line L2 for case M19 (a) and for case M18 (b), for different flow times. The results taken from Chen et al. [21] and Rodrigues et al. [22] and Lundh et al. [7] were added to the plot.

Case study M18 was simulated using the methodology proposed by Rodrigues et al. [22]. The air concentration profile obtained on line L2 for 600, 1000, 3000 and 10,000 s is depicted in Fig. A1 (b), together with the result presented by Rodrigues et al. [18] at 1000 s (twice the MHR time). At this flow time, both simulation results were very similar and predicted air concentration values below 0.6 m of tank height that were closely in line with the results obtained by Lundh et al. [7]. However, if the simulation were continued for another four MHR times, until 3000 s, the air profile curve would show an approximately constant value (around 2 ml/l) of air concentration above the outlet pipe, the average concentration in the tank being increased by 31% in comparison to 1000 s. Therefore, as in the case of M19, it was concluded that carrying out a transient simulation for two MHR times was also not sufficient for the purpose of reaching a quasi-steady solution.

Extending the simulation from 3000 s to 10,000 s produced only slight changes at the upper and lower ends of the air profile curve. Moreover, average air concentration in the tank increased asymptotically only by 3%. Therefore, as speculated by Bondelind et al. [20], the results showed a flow structure that was time dependent at the beginning of the simulation although when the general flow pattern was established, the solution became almost independent of time. Hence, the solution for 10,000 s can be assumed to be the quasi-steady solution, while the solution for 3000 s is so close to the latter that it can be considered a good approximation.

Finally, the most important finding in this benchmark was that steady-state simulation provided a solution that was very similar to the quasi-steady solution (see Fig. A1 (b)) albeit taking only a fraction of the computation time. The average air concentration in the tank obtained via steady-state simulation was only 1% higher than that calculated via transient simulation for 10,000 s. Therefore, carrying out steady-state simulations proved to be a suitable approach for the purpose of analysing DAF systems.

Appendix B. Comparison between Euler-Euler and Mixture models

The M18 and M19 cases were analysed using two multiphase models, namely, the Euler-Euler and Mixture models. It should be pointed out that in order to compare both models, the same two forces were included (Drag and Buoyancy) in the Euler-Euler approach. Four different bubble diameters (57, 67, 77 and 87 µm) were used in the study. Air contours along with the water velocity vectors can be found in Fig. B1. Simulations have evidenced very similar distribution of the air phase and velocity vector fields from the qualitative point of view in the case of both models. The major changes were observed in the contours of critical diameter bubbles (see Fig. B1, c and g), because the flow structure was very sensitive to this bubble size. It is worth mentioning that the time and computational resource required to perform simulation via the Mixture approach were considerably lower, in comparison to the Euler-Euler approach. Air contours for M18 were not included because the results were also very similar.

Table B1
Air distribution and WWL position for different MB sizes in the case of Euler-Euler (*Eu—Eu*) and Mixture approaches. AAF is the volume-weighted average of air fraction and WWL is the white water level.

	M18	57 µm	67 µm	77 µm	87 µm
Eu-Eu	AAF	2.00E-03	1.90E-03	1.30E-03	4.70E-04
	WWL (m)	0.1	0.1	0.3	0.89
Mixture	AAF	2.00E-03	1.90E-03	1.30E-03	4.80E-04
	WWL (m)	0.1	0.1	0.3	0.89
	M19	57 µm	67 µm	77 µm	87 µm
Eu-Eu	AAF	3.40E-03	3.20E-03	2.90E-03	9.70E-04
	WWL (m)	0.1	0.1	0.13	0.9
Mixture	AAF	3.50E-03	3.20E-03	2.80E-03	9.70E-04
	WWL (m)	0.1	0.1	0.14	0.89

The WWL position and volume-weighted average of air fraction values were compared between the Euler-Euler and Mixture models (see Table B1)

in the case of M18 and M19. It is worth noting that Table B1 reinforces the conclusions reached for Fig. B1. Volume-weighted average of air fraction was calculated for different bubble diameters inside the DAF tank domain, providing practically identical values in the case of both models. Additionally, WWL was determined, and the results were very similar, and it was concluded that both models were equally valid for the purpose of performing DAF tank simulations.
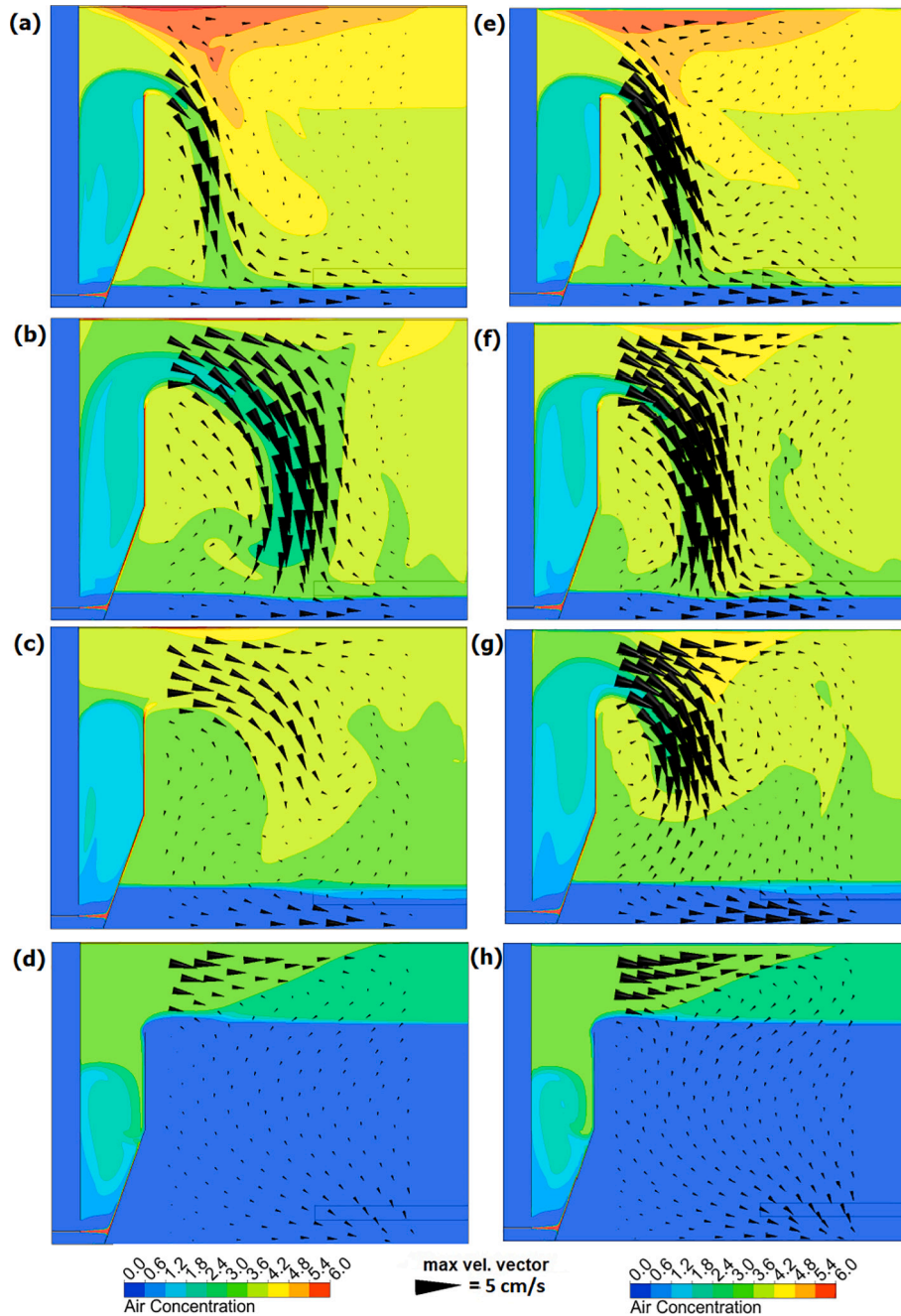

Fig. B1. M19 case simulated using Euler-Euler (a-d) and Mixture (e-h). The contours show air phase distribution along with water velocity vectors for different bubble diameters: 57 μm (a, e), 67 μm (b, f), 77 μm (c, g), 87 μm (d, h).

References

[1] S.B. Kwon, N.S. Park, S.J. Lee, H.W. Ahn, C.K. Wang, Examining the effect of length/width ratio on the hydro-dynamic behaviour in a DAF system using CFD and ADV techniques, Water Sci. Technol. 53 (2006) 141–149, https://doi.org/10.2166/wst.2006.218.

[2] J. Haarhoff, L.Van Vuuren, A South African design guide for dissolved air flotation: report for the water research commission, Water Research Commission (1993). Report TT 60/93.

[3] J.R. Crittenden, R. Trussell, D.W. Hand, K.J. Howe, G. Tchobanoglous, MWH Water Treatment Principles and Design, Third edition, 2012. http://link.springer.com/10.1007/s10337-013-2600-x.

[4] J.K. Edzwald, Dissolved air flotation and me, Water Res. 44 (2010) 2077–2106, https://doi.org/10.1016/j.watres.2009.12.040.

[5] M. Lundh, L. Jonsson, J. Dahlquist, Evaluation of an ejector-based air saturation system for dissolved air flotation, Vatten 58 (2002) 119–124.

[6] M. Lundh, Effects of Flow Structure on Particle Separation in Dissolved Air Flotation, Lund University, Water and Environmental Engineering, Box 118, 221 00 Lund, Sweden, 2002.

[7] M. Lundh, L. Jönsson, J. Dahlquist, The flow structure in the separation zone of a DAF pilot plant and the relation with bubble concentration, Water Sci. Technol. 43 (2001) 185–194, https://doi.org/10.2166/wst.2001.0493.

[8] M. Lundh, L. Jonsson, J. Dahlquist, The influence of contact zone configuration on the flow structure in a dissolved air flotation pilot plant, Water Res. 36 (2002) 1585–1595, https://doi.org/10.1016/S0043-1354(01)00357-8.

[9] M. Lundh, L. Jönsson, Residence time distribution characterization of the flow structure in dissolved air flotation, J. Environ. Eng. 131 (2005) 93–102, https://doi.org/10.1061/(ASCE)0733-9372(2005)131:1(93).

[10] M. Lundh, L. Jönsson, J. Dahlquist, Experimental studies of the fluid dynamics in the separation zone in dissolved air flotation, Water Res. 34 (2000) 21–30, https://doi.org/10.1016/S0043-1354(99)00136-0.

[11] T. Amato, J. Wicks, The practical application of computational fluid dynamics to dissolved air flotation, water treatment plant operation, design and development, J. Water Supply Res. Technol. AQUA 58 (2009) 65–73, https://doi.org/10.2166/aqua.2009.003.

[12] J.K. Edzwald, Principles and applications of dissolved air flotation, Water Sci. Technol. 31 (1995) 1–23, https://doi.org/10.1016/0273-1223(95)00200-7.

[13] K. Fukushi, N. Tambo, Y. Matsui, Flotation in water and wastewater treatment, Water Sci. Technol. 31 (1995) 37–47, https://doi.org/10.1016/0273-1223(95)00202-X.

[14] E.M. Rykaart, J. Haarhoff, Behaviour of air injection nozzles in dissolved air flotation, Water Sci. Technol. 31 (1995) 25–35, https://doi.org/10.1016/0273-1223(95)00201-W.

[15] J.K. Edzwald, J. Haarhoff, Dissolved Air Flotation For Water Clarification, McGraw-Hill Education, 2011. https://books.google.es/books?id=rAhMqYSdMAAC.

[16] J. Hague, C.T. Ta, M.J. Biggs, J.A. Sattary, Small scale model for CFD validation in DAF application, Water Sci. Technol. 43 (2001) 167–173, https://doi.org/10.2166/wst.2001.0491.

[17] Y. Wang, W. Liu, Z. Du, A. Zhou, L. Tian, R. Jia, Research on the CFD numerical simulation and process optimization of countercurrent-cocurrent dissolved air flotation, J. Water Supply Res. Technol. AQUA 68 (2019) 325–336, https://doi.org/10.2166/aqua.2019.147.

[18] L. Li, Z. Sun, R. Zhang, Numerical simulation of sedimentation processes in a novel air flotation-sedimentation tank, J. Water Process Eng. 18 (2017) 41–46, https://doi.org/10.1016/j.jwpe.2017.05.006.

[19] G. Wang, L. Ge, S. Mitra, G.M. Evans, J.B. Joshi, S. Chen, A review of CFD modelling studies on the flotation process, Miner. Eng. 127 (2018) 153–177, https://doi.org/10.1016/j.mineng.2018.08.019.

[20] M. Bondelind, S. Sasic, T.J.R. Pettersson, T.D. Karapantsios, M. Kostoglou, L. Bergdahl, Setting up a numerical model of a DAF tank: turbulence, geometry, and bubble size, J. Environ. Eng. 136 (2010) 1424–1434, https://doi.org/10.1061/(ASCE)EE.1943-7870.0000275.

[21] A. Chen, Z. Wang, J. Yang, Influence of bubble size on the fluid dynamic behavior of a DAF tank: a 3D numerical investigation, Colloids Surf. A Physicochem. Eng. Asp. 495 (2016) 200–207, https://doi.org/10.1016/j.colsurfa.2015.10.039.

[22] J.P. Rodrigues, R. Béttega, Evaluation of multiphase CFD models for dissolved air flotation (DAF) process, Colloids Surf. A Physicochem. Eng. Asp. 539 (2018) 116–123, https://doi.org/10.1016/j.colsurfa.2017.12.015.

[23] L. Tang, S. Zhang, M. Li, X. Zhang, Z. Wu, L. Ma, in: Numerical Investigation on the Dynamic Flow Pattern in a New Wastewater Treatment System, 2021, pp. 1–13.

[24] B. Deng, Q. Ding, D. Ge, Three dimensional eulerian-eulerian simulation on hydrodynamics in dissolved air flotation tank with different turbulence models, Water Sci. Technol. 76 (2017) 425–433, https://doi.org/10.2166/wst.2017.178.

[25] T. Amato, J. Wicks, Dissolved air flotation and potential clarified water quality based on computational fluid dynamics modelling, Water Qual. Technol. Conf. Expo. 2009 (2009) 459–473, https://doi.org/10.13140/2.1.2605.2480.

[26] M. Bondelind, S. Sasic, M. Kostoglou, L. Bergdahl, T.J.R. Pettersson, Single- and two-phase numerical models of dissolved air flotation: comparison of 2D and 3D simulations, Colloids Surf. A Physicochem. Eng. Asp. 365 (2010) 137–144, https://doi.org/10.1016/j.colsurfa.2010.02.035.

[27] K. Satpathy, U. Rehman, B. Cools, L. Verdickt, G. Peleman, I. Nopens, CFD-based process optimization of a dissolved air flotation system for drinking water production, Water Sci. Technol. 81 (2020) 1668–1681, https://doi.org/10.2166/wst.2020.028.

[28] V. Emmanouil, E.P. Skaperdas, T.D. Karapantsios, K.A. Matis, Two-phase simulations of an off-nominally operating dissolved-air flotation tank, Int. J. Environ. Pollut. 30 (2007) 213–230, https://doi.org/10.1504/IJEP.2007.014701.

[29] M. Ishii, K. Mishima, Two-fluid model and hydrodynamic constitutive relations, Nucl. Eng. Des. 82 (1984) 107–126, https://doi.org/10.1016/0029-5493(84)90207-3.

[30] C.E. Brennen, Fundamentals of Multiphase Flow, Cambridge University Press, 2005, https://doi.org/10.1017/CBO9780511807169.

[31] B. Lakghomi, Y. Lawryshyn, R. Hofmann, Importance of flow stratification and bubble aggregation in the separation zone of a dissolved air flotation tank, Water Res. 46 (2012) 4468–4476, https://doi.org/10.1016/j.watres.2012.05.038.

[32] M. Manninen, V. Taivassalo, S. Kallio, On the Mixture Model for Multiphase Flow 3–67, VTT Publ., 1996.

[33] J.R.G.R. Clift, Bubbles, Drops and Particles, Academic Press, New York, 1978, https://doi.org/10.1017/S0022112079221290.

[34] J. Hague, C.T. Ta, M.J. Biggs, J.A. Sattary, Small scale model for CFD validation in DAF application, Water Sci. Technol. 43 (2001) 167–173, https://doi.org/10.2166/wst.2001.0491.

[35] M.A. Park, K.H. Lee, J.D. Chung, Effects of turbulence models on micro-bubble distribution in dissolved air flotation process for water treatment, The Asian Conference on Sustainability, Energy, and the Environment (2015).

[36] C.T. Ta, J. Beckley, A. Eades, A multiphase CFD model of DAF process, Water Sci. Technol. 43 (2001) 153–157, https://doi.org/10.2166/wst.2001.0488.

[37] I.B. Celik, U. Ghia, P.J. Roache, C.J. Freitas, H. Coleman, P.E. Raad, Procedure for estimation and reporting of uncertainty due to discretization in CFD applications, J. Fluids Eng. Trans. ASME 130 (2008) 0780011–0780014, https://doi.org/10.1115/1.2960953.

[38] P.T.L. Koh, M.P. Schwarz, Modelling attachment rates of multi-sized bubbles with particles in a flotation cell, Miner. Eng. 21 (2008) 989–993, https://doi.org/10.1016/j.mineng.2008.02.021.

[39] A.R. Sarhan, J. Naser, G. Brooks, CFD simulation on influence of suspended solid particles on bubbles' coalescence rate in flotation cell, Int. J. Miner. Process. 146 (2016) 54–64, https://doi.org/10.1016/j.minpro.2015.11.014.

[40] M.J. Prince, H.W. Blanch, in: Bubble Coalescence and Break-up in Air-sparged Bubble Columns 36, 1990, pp. 1485–1499.

[41] H. Luo, H.F. Svendsen, Theoretical model for drop and bubble breakup in turbulent dispersions, AIChE J. 42 (1996) 1225–1233, https://doi.org/10.1002/aic.690420505.

[42] J.P. Rodrigues, J.N.M. Batista, R. Béttega, Application of population balance equations and interaction models in CFD simulation of the bubble distribution in dissolved air flotation, Colloids Surfaces A Physicochem. Eng. Asp. 577 (2019) 723–732, https://doi.org/10.1016/j.colsurfa.2019.06.032.